Secondary neutron-production cross sections from heavy-ion interactions in composite targets

L. Heilbronn,[1,*] Y. Iwata,[2] H. Iwase,[3,†] T. Murakami,[2] H. Sato,[3,‡] T. Nakamura,[3] R. M. Ronningen,[4] K. Ieki,[5] I. Gudowska,[6] and N. Sobolevsky[7]

[1]*MS 74-197, Lawrence Berkeley National Laboratory, Berkeley, California 94720, USA*

[2]*Department of Accelerator Physics and Engineering, National Institute of Radiological Sciences, 4-9-1 Anagawa, Inage, Chiba 263-8555, Japan*

[3]*Cyclotron and Radioisotope Center, Tohoku University, Aoba, Aramaki, Sendai 980-8578, Japan*

[4]*National Superconducting Cyclotron Laboratory, Michigan State University, East Lansing, Michigan 48824-1321, USA*

[5]*Department of Physics, Rikkyo University, 3-34-1 Nishi Ikebukuro, Toshima, Tokyo 171-8501, Japan*

[6]*Department of Medical Radiation Physics, Karolinska Institutet and Stockholm University, Box 260, S-171 76 Stockholm, Sweden*

[7]*Department of Neutron Research, Institute for Nuclear Research of the Russian Academy of Sciences, RU-117312 Moscow, Russia*

(Received 16 March 2005; published 13 February 2006)

Secondary neutron-production cross sections have been measured from interactions of 290 MeV/nucleon C and 600 MeV/nucleon Ne in a target composed of simulated Martian regolith and polyethylene, and from 400 MeV/nucleon Ne interactions in wall material from the International Space Station. The data were measured between 5° and 80° in the laboratory. We report the double-differential cross sections, angular distributions, and total neutron-production cross sections from all three systems. The spectra from all three systems exhibit behavior previously reported in other heavy-ion neutron-production experiments, namely, a peak at forward angles near the energy corresponding to the beam velocity, with the remaining spectra generated by pre-equilibrium and equilibrium processes. The double-differential cross sections are fitted with a moving-source parametrization. Also reported are the data without corrections for neutron flux attenuation in the target and other intervening materials and for neutron production in nontarget materials near the target position. These uncorrected spectra are compared with SHIELD-HIT and PHITS transport model calculations. The transport model calculations reproduce the spectral shapes well but, on average, underestimate the magnitudes of the cross sections.

DOI: 10.1103/PhysRevC.73.024603 PACS number(s): 25.70.Mn

I. INTRODUCTION

The establishment of a permanent human presence in space has been a long-term vision for humans. It has been partially realized with the International Space Station (ISS), and plans are being made for the exploration and settlement of the moon and Mars. One of the limiting factors to long-term human activities in space is the health risk to astronauts from exposure to the ionizing-radiation environment of space. The ultimate limitation on long-term operations is maintaining the radiation-induced cancer risks to acceptable levels. The most effective method to decrease radiation exposure is the use of intervening materials to reduce the radiation intensity within an enclosed structure.

The National Aeronautics and Space Administration (NASA) of the United States is currently supporting a ground-based research program to study the effects of galactic cosmic radiation (GCR) transport through spacecraft materials and human tissue. The goal of the program is to provide a reliable database of relevant nuclear cross sections and thick target yields for the development and verification of transport model calculations used for shielding designs applicable to both low-Earth orbit and deep space. Any advances on the specification of shielding in spacecraft or for habitats on the moon or Mars require measurements on the transmitted neutron component within candidate shielding materials.

The ionizing-radiation environment of space is very complex, consisting of a low-level background of GCR, transient solar particle events (SPE), and, in Earth orbit, belts of trapped radiation [1,2]. As these radiations traverse shielding materials they interact with the materials through specific atomic and nuclear processes, including breaking up the ions into smaller fragments and producing secondary radiation that can penetrate more deeply into the material. An important component of the secondary-particle radiation field is the neutron, which is deeply penetrating and can be extremely damaging to biological tissue. Current theoretical models have shown the secondary neutrons to be a significant contributor to exposures within lunar habitats and on the Martian surface [3], and recent studies have shown that neutrons could comprise up to 30% of the dose equivalent on the ISS [4].

The peak of the GCR flux occurs between 200 and 600 MeV/nucleon, independent of the species of ion. GCR energies can go to several TeV/nucleon, but in general most of the flux is contained between 50 MeV/nucleon and a few GeV/nucleon. Because of the complexity of the radiation environment in space, it is impossible to measure the effectiveness of every candidate shielding material for every possible mission scenario using ground-based accelerator measurements. The determination of shield effectiveness and, ultimately, the radiation risk to humans in space will come from transport model calculations used together with models

*E-mail: LHHeilbronn@LBL.gov

†Present address: Gesellschaft für Schwerionenforschung, Darmstadt, Germany.

‡Present address: Isogo Nuclear Engineering Center, Toshiba Co., 8 Shinsugita-Cho, Isogo-Ku, Yokohama 235-8523, Japan.

of biological response to radiation. Both deterministic and Monte Carlo approaches can be applied to transport model calculations. A deterministic approach for heavy-ion transport in complex media has undergone development at the NASA Langley Research Center since the mid 1980s. It has yielded a family of radiation transport codes mainly dedicated to solving engineering problems in radiation-shielding analysis for space missions [5–7]. One of these deterministic codes is the high-charge-and-energy transport code HZETRN, based on the one-dimensional formulation of the Boltzmann transport equation with a straight-ahead approximation [8] and a semi-empirical abrasion-ablation fragmentation model for nuclear fragmentation processes. Using simplifying approximations, this code can provide the radiation field in and around shielding materials with an acceptable accuracy for space research.

Several Monte Carlo computer codes exist, or are in the stage of development, for the simulation of the transport of light and heavy ions in matter. Two codes for the simulation of hadronic cascades (neutrons, protons, and pions), HETC [9] and SHIELD [10], were developed in the early 1970s in the United States (Oak Ridge) and the former USSR (Dubna), respectively. The original HETC code was based on Bertini's model of intranuclear cascades [11]; SHIELD used the Dubna cascade-evaporation model of nuclear reactions [12]. These two codes have evolved considerably, and whereas SHIELD has kept its original name until today, various spin-offs of HETC have proliferated under the names of HERMES [13], LAHET [14], MCNPX [15], NMTC/JAERI [16], and PHITS [17,18]. Other major Monte Carlo transport codes currently in use (but not utilized in this paper) are MARS [19], FLUKA [20,21], and GEANT3 [22]. The authors of these codes are in the process of incorporating heavy-ion transport for all energies above at least 100 MeV/nucleon, if they have not done so already.

The validation and verification of the output from transport model calculations depends on a reliable set of experimental nuclear data with which to compare. Until recently, the amount of thin-target (cross sections) and thick-target (yields) neutron-production data from heavy-ion interactions that was applicable to the general problem of GCR transport was scant. A number of thick-target (stopping-target) neutron yields from high-energy (<100 MeV/nucleon) heavy-ion experiments have been published [23–28] and these can be used for direct confirmation of transport model calculations of various components of the GCR field. Also, there are some existing heavy-ion, neutron-production cross-section measurements relevant to GCR transport [29–34].

In this paper we present neutron-production cross sections from two specialized NASA targets: (1) A slab of simulated Martian regolith mixed with polyethylene, referred to herein as "marsbar," and (2) a section of wall from the ISS. As opposed to the previously mentioned measurements, the two targets used here are composed of more than one element, and as such they add another degree of complexity to the transport model's calculating ability to reproduce secondary-particle spectra. In addition to the neutron-production cross sections, the data are also presented without corrections for neutron flux attenuation through the target and other intervening materials or for neutron production in nontarget materials that are near the target position. Because transport model calculations incorporate the effects of attenuation and nontarget production, SHIELD-HIT and PHITS calculations are compared with the uncorrected data.

II. EXPERIMENTAL DETAILS

The measurements took place in April 2000 at the Heavy Ion Medical Accelerator in Chiba (HIMAC) facility of the National Institute of Radiological Sciences (NIRS), Japan. Beams of 290 MeV/nucleon C, 400 MeV/nucleon Ne, and 600 MeV/nucleon were produced by HIMAC and transported to the SB3 beam course. A schematic diagram of the experimental setup in that beam course is shown in Fig. 1.

Beam pulses were delivered on target every 3.3 s. Pulse length varied from 0.5 to 1 s, depending on beam ion and energy. Typical pulse intensities varied between 10^4 and 10^5 particles per pulse. The beam spot size was a few millimeters in diameter. The beam divergence was negligible compared with the spread of the beam from Coulomb scattering by the target and air constituents. The beam exited the vacuum beam line through a 100-μm-thick aluminum window and passed through a 0.5-mm-thick, 3-cm diameter NE102A scintillator placed approximately 5 cm downstream from the exit window. That scintillator, referred to as the trigger detector, was used to count the number of beam particles incident upon the target. It was also used to provide a timing signal for a time-of-flight measurement with each event in the neutron detectors.

After passing through the trigger detector, the beam then passed through the target position, approximately 10 cm downstream from the exit window. The targets used in these

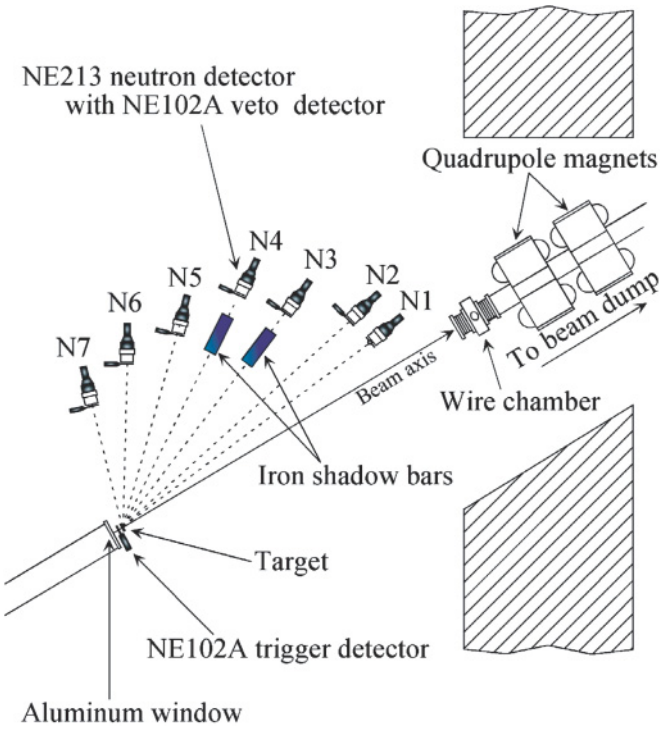

FIG. 1. (Color online) A schematic diagram of the experimental setup on the SB3 beam course at HIMAC. The quadrupole magnets are positioned at a concrete shielding wall separating the target hall from the shield room where the beam dump was located.

TABLE I. Martian regolith composition.

Element	Atomic density (atoms/g)
O	1.67×10^{22}
Mg	1.62×10^{21}
Si	5.83×10^{21}
Ca	7.81×10^{20}
Fe	1.80×10^{21}

measurements were provided by NASA's Langley Research Center. The target used with the 290 MeV/nucleon C and 600 MeV/nucleon Ne beams was a 5.0 g/cm^2 thick (2.5-cm-thick), 10-cm by 10-cm composite brick made of 85% (by weight) simulated Martian regolith and 15% polyethylene, referred to herein as "marsbar." The marsbar is regarded as a reasonable approximation of what may be used for habitat construction on the surface of Mars: bricks composed of Martian soil, with a polymer binder produced by mixing components of Mars' CO_2 atmosphere and water. Table I shows a breakdown of the elemental composition of Martian soil. Factoring in the percentages (by weight) of polyethylene and regolith in the marsbar target gives a total of 4.20×10^{22} atoms per gram of target. The marsbar is thick enough to produce an appreciable energy loss as the beam traverses through the target. The C beam has an incident energy of 290 MeV/nucleon and an exit energy of 240 MeV/nucleon (with a median energy of 265 MeV/nucleon). The Ne beam has an incident energy of 600 MeV/nucleon and an exit energy of 540 MeV/nucleon (with a median energy of 570 MeV/nucleon). Based on previous measurements [34] it is believed that the cross sections will not vary much over the range of beam energies present through the target.

The target used for the 400 MeV/nucleon Ne measurements is a section of the wall used in some parts of the ISS. It is regarded as an example of typical material for the design of transit vehicles and orbital vehicles used in space exploration. The ISS wall is composed of 1.89 g/cm^2 of aluminum, 0.218 g/cm^2 of Nomex® honeycomb wall, 0.08 g/cm^2 of Nomex® cloth, 0.06 g/cm^2 Durette® batting, and 0.72 g/cm^2 silicone rubber. The 1.89 g/cm^2 aluminum is a combination of two pieces: an outer "bumper" hull and an inner pressure wall. Like the marsbar target, the ISS wall target was 10 cm wide and 10 cm high. The 400 MeV/nucleon Ne beam incident upon the ISS wall has an exit energy of 360 MeV/nucleon (with a median energy of 380 MeV/nucleon).

After passing through the target, the beam then traveled approximately 20 m before stopping in a beam dump located in a second shielded room, downstream from the primary experimental hall. A set of quadrupole magnets, located about 7 m downstream from the target at the concrete shielding partition between the two halls, was used to focus the beam into the beam dump. A shield constructed of iron blocks was used to reduce possible "back-shine" of radiation from the beam dump to the neutron detectors at forward angles.

Seven liquid-scintillator (NE213) neutron detectors were placed in the laboratory between 5° and 80°, at varying flight paths from the target position. Table II contains information regarding the positions of each detector. The flight path lengths

TABLE II. Neutron detector information. The uncertainty in the solid angle is reported as a percentage.

Detector	Flight path length (cm)	Laboratory angle (deg)	Solid angle (msr)
N1	506	5	$0.494 \pm 5.0\%$
N2	506	10	$0.494 \pm 5.0\%$
N3	456	20	$0.608 \pm 5.6\%$
N4	456	30	$0.608 \pm 5.6\%$
N5	406	40	$0.767 \pm 6.2\%$
N6	356	60	$0.998 \pm 7.1\%$
N7	306	80	$1.35 \pm 8.3\%$

listed in Table II indicate the distance from target center to detector center, in centimeters. The neutron detectors are cylindrical cells 12.7 cm in diameter and 12.7 cm long, oriented such that the cylindrical axis was along the line connecting the target center to the detector center. Each detector cell was directly coupled to a 12.7-cm-diameter phototube. The intrinsic timing resolution of these detectors, as measured with a ^{60}Co source, is on the order of 700–800 ps.

A 5-mm thick, 12.7-cm by 12.7-cm square, solid plastic (NE102A) scintillator (referred to as a "veto detector") was placed in front of each neutron detector. The veto detectors were used to tag events in the neutron detectors that came from charged particles produced in the target. The veto detectors were thin enough that events where a neutron or γ ray interacted in the veto detector and registered in the companion neutron detector were ignored in the offline analysis.

Periodically during the experiment, iron bars were placed in front of the neutron detectors. The iron bars, referred to as "shadow bars," were 60 cm long and 15 cm by 15 cm square. When placed in front of a neutron detector, the shadow bar blocks neutrons coming directly from the target, allowing only background neutrons to enter the detector. Background neutrons include neutrons scattered off the floor, walls, ceilings, and other materials placed in the target and beam-dump halls. Two shadow bars were used, and their positions were shifted from detector to detector during the measurements to ensure that each neutron detector had an adequate determination of its background spectrum. Event rates in detectors with a shadow bar in front of a neighboring detector were checked against event rates when that same detector had no shadow bar nearby. It was determined that outscattering from the shadow bars had a negligible effect on the measurements made in neighboring, unshadowed detectors.

Data were acquired on an event-by-event basis. Acquisition live times varied between 60% and 90%. The trigger for a valid event was a coincidence between a signal in the trigger detector and a signal in one (or more) of the neutron detectors. For each event, the following information was recorded: (1) the magnitude of the signal from the trigger detector, as measured by a charge-integrating analog-to-digital converter (QDC); the magnitudes of the (2) total and (3) slow components of the pulse from the neutron detector's photomultiplier tubes, as measured by a QDC; (4) the time difference between the signal from the trigger detector and the trigger-event coincidence gate, as measured with a time-to-digital converter (TDC); and

(5) the "self-time" difference between the signal from neutron detector and the trigger-event gate signal. For a discussion of the information contained in (2) and (3), see Ref. [35].

III. ANALYSIS DETAILS

A. Neutron-energy determination

Neutron energies were determined by the time-of-flight method, using the signals from the neutron detectors and trigger detector as the start and stop signals, respectively. For each event, the neutron detector in which the event occurred was identified using a self-time signal. For this analysis, events in which two or more neutron detectors gave a valid self-time signal were excluded. Those events accounted for less than 2% of the total number of events. Neutron velocities were calculated using the flight paths given in Table II and the flight times determined from the trigger/neutron-detector TDC data. An absolute time scale in each neutron detector's TDC spectrum was determined by locating the position of the prompt γ-ray peak in the TDC spectrum. Prompt γ rays refer to γ rays produced in the target by direct interactions between the beam and target material. The overall timing resolution, as determined by the full width at half-maximum of the prompt γ-ray peak, was on the order of 1 ns for all seven detectors. The overall timing resolution includes effects such as constant-fraction-discriminator (CFD) walk and signal noise folded with the intrinsic timing resolution of each detector. Where possible, the data were corrected for excessive CFD walk by using an offline analysis technique [36]. The minimum TDC binwidth was set to 1 ns in the offline analysis.

The overall energy resolution is a function of the neutron energy and can be calculated by using the following equation from Ref. [34]:

$$\frac{\Delta E_n}{E_n} = \frac{E_n + M_n}{E_n} \frac{\beta^2}{1-\beta^2} \sqrt{\left(\frac{\Delta L}{L}\right)^2 + \left(\frac{\Delta t}{t}\right)^2}, \qquad (1)$$

where Δt refers to the overall timing resolution, t refers to the time of flight, L refers to the flight path, E_n and β refer to the usual kinematical quantities, M_n is the neutron rest mass (in MeV/$c^{2)}$, and ΔL refers to the thickness of the neutron detector (12.7 cm). For the 5° and 10° detectors, where the spectra are dominated by high-energy neutrons, the energy resolutions for 200-, 400-, and 600-MeV neutrons are approximately 8%, 11%, and 14%, respectively. A more complete listing of energy resolutions for all seven detectors may be found in Ref. [34].

B. Discrimination of neutron events from other events

Charged-particle events were excluded by using information from the veto detectors. Gamma-ray events were separated from neutron events by using the pulse-shape properties of NE-213 liquid scintillators [35]. By plotting the total QDC pulse (Q_{tot}) versus the slow component of the pulse (Q_{slow}), two clearly separated lines corresponding to γ-ray events and neutron events can be seen. An example of such a plot may be seen in Ref. [34]. Background neutrons were subtracted offline by using data taken when the shadow bars were directly in front of the detectors.

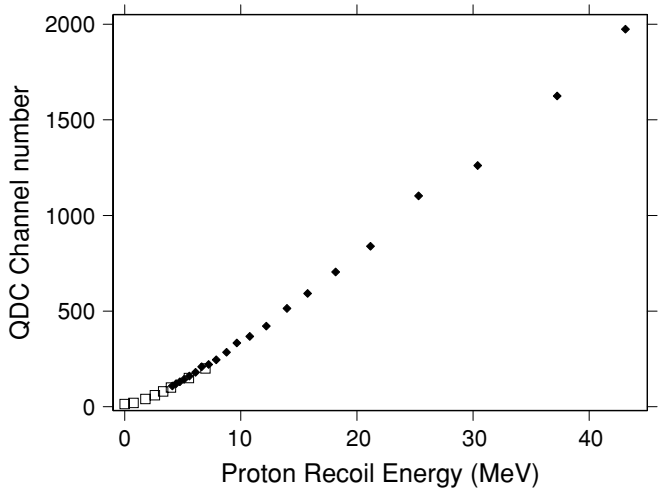

FIG. 2. Pulse-height-to-energy calibration of the charge-integrating analog-to-digital converter. The open, square symbols show the fit to the Compton-edge data, and the closed, diamond-shaped symbols show the data from the maximum-recoil method.

C. QDC calibration

Threshold cuts were applied to the QDC spectra to correct for the neutron-detection efficiency. The QDC spectra were calibrated with two methods: (1) using ^{60}Co and AmBe sources to produce Compton spectra, and converting the electron-equivalent MeV (MeVee) values to MeV, and (2) plotting QDC versus TDC for neutron events, identifying the points of maximum recoil energy (see Ref. [27] for details), and converting the corresponding TDC values to energy, in MeV. The Compton spectra provide a good calibration at lower energies, whereas the maximum-recoil method provides a good calibration at higher energies. Figure 2 shows a plot of the QDC calibration for detector N1. The square symbols show the fit to the Compton edge spectra, and the diamond-shaped symbols show the calibration using the maximum-recoil method. Good agreement is seen in the area of overlap between the two methods. The uncertainty in the QDC calibration, as determined by multiple trials with both methods, is ± 15 channels.

D. Normalization

Cross sections were normalized to the number of incoming beam particles. The number of incident beam particles was counted using the trigger detector. Events in which the trigger detector fired more than once during the trigger-detector/neutron-detector coincidence were excluded from the analysis, and the number of beam particles in those events were excluded from the normalization.

To express the cross sections in units of barns, the data were also normalized to the number of scattering sites per unit area. For both targets used, each atomic constituent of the material was considered a scattering site. Thus, for the marsbar target, a normalization factor of 0.2102 scattering sites per barn was calculated using the information from Table I, along with the reported ratio of polyethylene to marsbar in the target. For the ISS wall target, a normalization factor of 0.0632

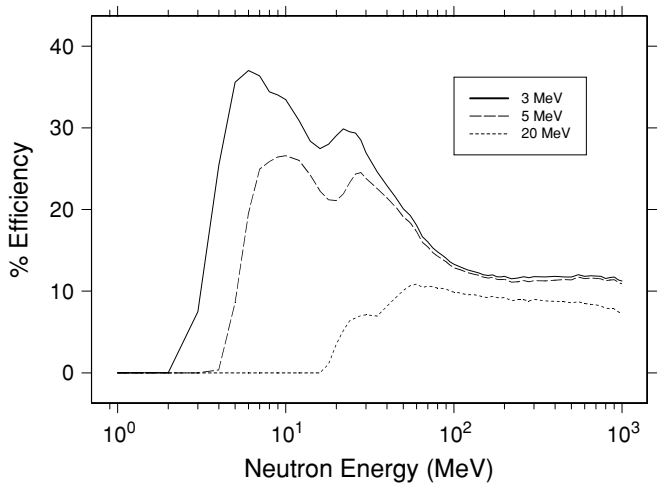

FIG. 3. Plot of neutron-detection efficiency (in percent) as a function of neutron energy. Efficiencies are shown for thresholds of 3 MeV (0.92 electron-equivalent MeV), 5 MeV (1.90 electron-equivalent MeV), and 20 MeV (11.5 electron-equivalent MeV) in neutron energy.

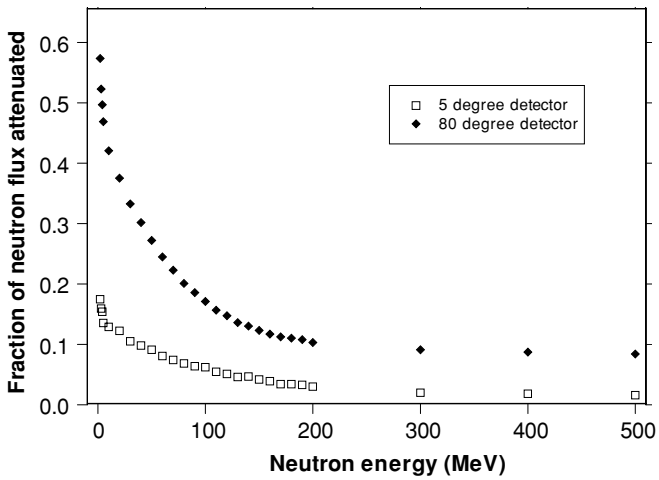

FIG. 4. An estimation of the fraction of neutron flux that does not make it to the neutron detector owing to absorption and out-scattering in the marsbar target and other intervening materials between the target and detector. The open, square symbols show the fraction lost from the detector at 5°, and the closed, diamond-shaped symbols show the fraction lost from the detector at 80°.

scattering sites per barn was calculated using information from the manufacturer. If one wishes to express the cross sections in units of number of neutrons per incoming ion per g/cm^2 of target, then (1) for the marsbar target, multiply cross sections expressed in barns by 0.042 (= 0.2102 ÷ 5.0 g/cm$^{2)}$ and (2) for the ISS wall target, multiply cross sections expressed in barns by 0.0213 (= 0.0632 ÷ 2.97 g/cm^2).

The neutron spectra were corrected for neutron-detection efficiency by using the code of Cecil *et al*. [37]. The uncertainty in the efficiency is taken to be 10%, based on previous experience [38] in comparisons of the Cecil code with another efficiency calculation, and based on the observations in Ref. [39]. Figure 3 shows the efficiency calculation for 3-, 5-, and 20-MeV thresholds.

E. Corrections applied to the cross sections

To estimate the effect of neutron flux attenuation on the spectra, the loss of neutron flux through the marsbar target was calculated using the energy-dependant half-value thicknesses (the thickness of material that will reduce the flux by one-half) for neutrons in concrete [40]. The marsbar target is similar in composition to concrete, and in the calculation it was assumed that the neutrons were produced at the midpoint of the target. In addition to the target, the attenuation of neutron flux through air and veto detector was also calculated using a code described in Ref. [38]. Figure 4 shows the result of the calculation for neutron flux measured at 5° and at 80°. The calculated attenuation is largest for low-energy neutrons at 80° (about 50% for 3-MeV neutrons), where the amount of target that is traversed is greatest. Similar results were obtained for calculations using the ISS wall target.

Just before striking the target, the beam passes through an exit window and beam scintillator (described in Sec. II). After passing through the target, the beam continues through an air column, eventually stopping in a beam dump well downstream from the target. Neutrons produced in the beam-course exit window, in the beam-trigger scintillator, and in parts of the air column are blocked when the shadow bars are in place, and as such they are not subtracted from the data when the shadow-bar correction is applied. Thus, it is possible for invalid neutrons (neutrons not from the target) to contaminate the measured spectra. The contribution of nontarget neutrons to the measured spectra is estimated here using the following equation:

$$P = \frac{\sum \rho_{\mathrm{nt}} t_{\mathrm{nt}} d\Omega_{\mathrm{nt}}}{\rho_{\mathrm{tgt}} t_{\mathrm{tgt}} d\Omega_{\mathrm{tgt}} + \sum \rho_{\mathrm{nt}} t_{\mathrm{nt}} d\Omega_{\mathrm{nt}}}, \tag{2}$$

where P is the estimated fraction of neutrons in the measured spectra that come from nontarget materials, ρ is the material density (with nontarget materials denoted by the subscript "nt" and target materials by "tgt"), t is the material thickness, and $d\Omega$ is the solid-angular acceptance at the point of production in those materials. The sum runs over all nontarget materials that contaminate the measured spectra (i.e., exit window, trigger detector, and air column). Table III shows the estimated percentage of neutron flux from nontarget materials in the measured spectra.

TABLE III. The estimated percentage of contamination in the measured spectra from neutrons produced in nontarget materials. The amount of contamination is shown for both targets used.

Detector	Marsbar target (%)	ISS Wall target (%)
N1 (5°)	22	33
N2 (10°)	22	32
N3 (20°)	19	28
N4 (30°)	13	21
N5 (40°)	7.9	13
N6 (60°)	3.8	6.3
N7 (80°)	2.3	3.8

F. Systematic uncertainties

The systematic uncertainties considered here are uncertainties in angular acceptance of the neutron detectors, neutron detection efficiency, QDC calibration, and the estimations described in Sec. III E. The uncertainties vary from detector to detector.

The angular acceptance of each detector depends on where the neutron interacts in the detector. The maximum acceptance occurs when the neutron interacts at the front face of the detector, and the minimum acceptance occurs when the interaction takes place at the back of the detector. Half of the difference between the front-face acceptance and the back-face acceptance is taken as the systematic uncertainty in the angular acceptance. Table II shows the solid angle subtended by each detector (in millisteradians), along with the percent uncertainty in each solid angle.

Another source of systematic uncertainty is the effect of the uncertainty in QDC calibration on threshold determination and its ultimate effect on the magnitude of the extracted cross sections. The uncertainty in the QDC calibration is ± 15 channels. To determine the effect that uncertainty has on the extracted cross sections, TDC spectra were generated for three thresholds: one threshold set at the calibrated QDC channel and two thresholds set at ± 15 QDC channels from the calibrated point. Double-differential spectra $d^2\sigma/(dE \cdot d\Omega)$ were then generated from the three TDC spectra by using the same detection-efficiency correction for all three. The spectra were then integrated over energy to produce $d\sigma/d\Omega$ spectra at each angle. The spread in $d\sigma/d\Omega$ over the three thresholds was used to quantify the systematic uncertainty in the precision of the threshold determination. The second column in Table III shows the percent systematic uncertainty in threshold precision for each detector.

The systematic uncertainty in the accuracy of the QDC calibration was estimated in the following manner: (1) Double-differential spectra were generated from data at each detector by using three different threshold settings. Typically, the thresholds used were 2, 5, and 20 MeV (in neutron energy). The appropriate efficiency file was used for each threshold. (2) The spectra were integrated over energy to produce $d\sigma/d\Omega$ spectra for each threshold and angle. (3) The $d\sigma/d\Omega$ yields from the three different threshold settings were compared with each other for each detector. To compare the $d\sigma/d\Omega$ yields at all three thresholds, a lower limit of 20 MeV was used when integrating the double-differential spectra. The third column in Table IV shows the percent systematic uncertainty in the extracted spectra owing to the uncertainty in the accuracy of the QDC calibration.

The systematic uncertainty in the attenuation calculation (Sec. III E) was estimated from comparisons with MCNP calculations. The two calculations disagreed by no more than 7%, and a conservative estimate of 10% in the uncertainty was determined from that value. The systematic uncertainty in the production of neutrons from nontarget materials [Eq. (2)] was dominated by the uncertainties in the determination of the amount of air that contributed to that production. The total uncertainty in nontarget production was estimated to be 15%.

The systematic uncertainties were applied to the angular distributions and total cross sections (next section). The total systematic uncertainty for a particular neutron detector was determined by adding the individual uncertainties in quadrature.

TABLE IV. Systematic uncertainties in the precision of the threshold determination (second column) and the accuracy of the threshold determination (third column). Percent uncertainties are shown.

Detector	Threshold precision (%)	Threshold accuracy (%)
N1 (5°)	±2.3	±4.7
N2 (10°)	±2.0	±5.0
N3 (20°)	±2.6	±2.8
N4 (30°)	±4.0	±4.9
N5 (40°)	±4.3	±8.0
N6 (60°)	±2.2	±3.1
N7 (80°)	±2.8	±7.4

IV. EXPERIMENTAL RESULTS

A. Double-differential spectra

Figure 5 shows the double-differential spectra from the 290 MeV/nucleon C + marsbar system. 290 MeV/nucleon is the energy incident upon the target; the beam energy at the midpoint of the target is 265 MeV/nucleon. Spectra from all seven angles are shown, along with the statistical uncertainties. The symbols show the data after all of the corrections previously described. The dashed line (red online) shows the data before the corrections for attenuation and for neutron production by nontarget materials. The spectrum at 5° is dominated by neutrons from the breakup of the projectile, resulting in a peak that is centered near the beam ion's specific energy (i.e., energy per nucleon). At 10° and 20°, evidence of neutrons from projectile-like fragments can still be seen, although the peaks are broader and centered at lower energies. At larger angles, the spectra appear to be generated from two distinct sources: (1) evaporation from the target residues that dominates the spectra below 20 MeV and (2) decay of the overlap region between the projectile and target that produce neutrons with energies from a few MeV up to hundreds of MeV.

Figure 6 shows the double-differential spectra from the 400 MeV/nucleon Ne + ISS wall system (400 MeV/nucleon incident upon the target, 380 MeV/nucleon at the midpoint of the target). Double-differential spectra from the 600 MeV/nucleon Ne + marsbar (570 MeV/nucleon at target midpoint) system are shown in Fig. 7. Only statistical uncertainties are shown. As with the 290 MeV/nucleon C + marsbar spectra, neutrons can be observed coming from a projectile-like source, a target-breakup source, and a pre-equilibrium source.

B. Angular distributions

Figures 8–10 show the angular distribution spectra for the 290 MeV/nucleon C, 400 MeV/nucleon Ne, and 600 MeV/nucleon Ne systems, respectively. The data points, shown with the symbols, were obtained by integrating the experimental double-differential spectra over energy for neutron energies greater than 3 MeV. The error bars include both

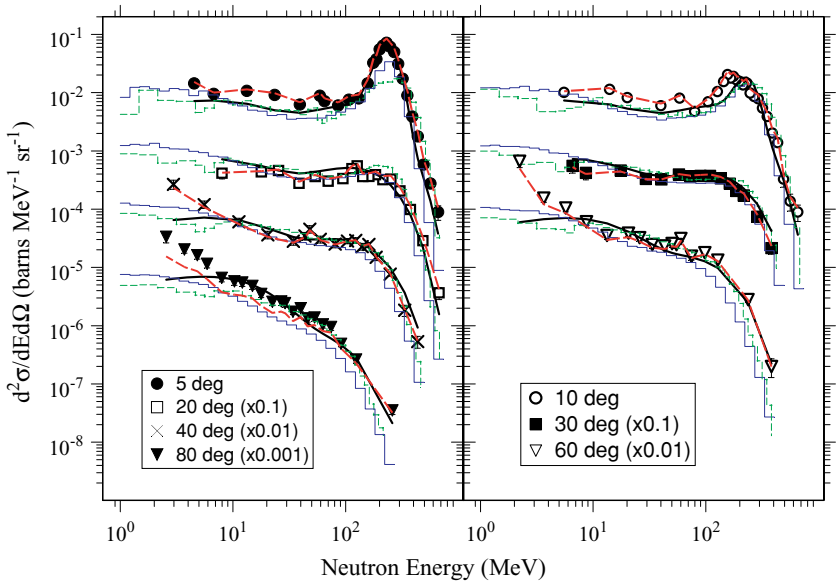

FIG. 5. (Color online) Double-differential neutron spectra from 290 MeV/nucleon C + marsbar, at the indicated laboratory angles. The error bars represent the statistical uncertainties. The symbols show the data after all of corrections described in Secs. III D and III E. The dashed (red) line shows the data before the corrections for attenuation and production from nontarget materials. The solid (black) lines show the fit to the data using a moving-source parametrization. The (green) dashed histograms show the results from a SHIELD-HIT calculation. Results from PHITS calculations are shown with the solid (blue) histograms. The spectra and fits are offset by successive factors of 10, as indicated in the legend.

statistical and systematic uncertainties. The solid lines show the fits to the data using the following parametrization:

$$d\sigma/d\Omega = a_1 \exp(-a_2\theta) + a_3 \exp(-a_4\theta), \qquad (3)$$

where θ is in degrees, and a_1, a_2, a_3, and a_4 are the fit parameters. Table V shows the fitted parameters from all three systems. The dashed lines (red online) show the data without corrections for attenuation and for production from nontarget materials. The dotted (blue online) and dot-dashed (green online) lines come from calculations described in Sec V.

C. Total cross sections

Table VI contains the total cross sections, in barns, from all three systems. The total cross sections are obtained for both the corrected and uncorrected data. The values were obtained by integrating the experimental double-differential spectra over energy (for energies above 3 MeV) and over angles from 0° to 90°. The data at 5° were integrated from 0° to 7.5°; the 10° data were integrated from 7.5° to 15°; the 20° data were integrated from 15° to 25°; the 30° data were integrated from 25° to 35°; the 40° data were integrated from 35° to 50°; the 60° data were integrated from 50° to 70°; and the 80° data were integrated from 70° to 90°. The uncertainties include both statistical and systematic uncertainties. The statistical uncertainties are on the order of 1–2%.

The total yields of neutrons per unit target mass, expressed in units of number of neutrons per incoming ion per g/cm^2 of target, are also reported in Table VI for the corrected data only. Those numbers were obtained by multiplying the values in the second column by the conversion factors reported in Sec. III C.

V. MODEL COMPARISONS

A. Moving-source parametrization

The solid lines in Figures 5–7 show the fits to the corrected data using a moving source parametrization. Three sources

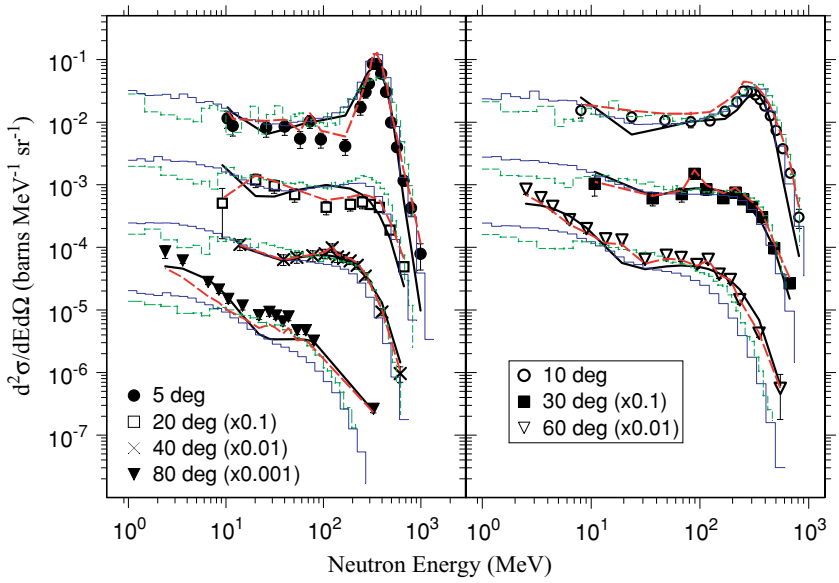

FIG. 6. (Color online) Double-differential neutron spectra from 400 MeV/nucleon Ne + ISS wall, at the indicated laboratory angles. The error bars represent the statistical uncertainties. The symbols show the data after all of corrections described in Secs. III D and III E. The dashed (red) line shows the data before the corrections for attenuation and production from nontarget materials. The solid (black) lines show the fit to the data using a moving-source parametrization. The (green) dashed histograms show the results from a SHIELD-HIT calculation. Results from PHITS calculations are shown with the solid (blue) histograms. The spectra and fits are offset by successive factors of 10, as indicated in the legend.

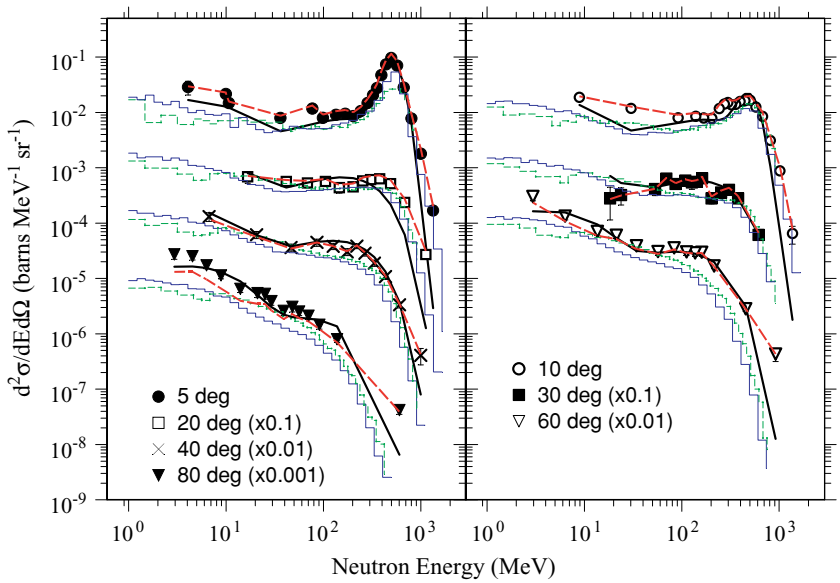

FIG. 7. (Color online) Double-differential neutron spectra from 600 MeV/nucleon Ne + marsbar, at the indicated laboratory angles. The error bars represent the statistical uncertainties. The symbols show the data after all of corrections described in Secs. III D and III E. The dashed (red) line shows the data before the corrections for attenuation and production from nontarget materials. The solid (black) lines show the fit to the data using a moving-source parametrization. The (green) dashed histograms show the results from a SHIELD-HIT calculation. Results from PHITS calculations are shown with the solid (blue) histograms. The spectra and fits are offset by successive factors of 10, as indicated in the legend.

were assumed in the fitting: (1) breakup of the projectile, (2) breakup of the decay of the overlap region, and (3) decay of the target remnant.

As was done in Ref. [34], the projectile-like source was assumed to have the form

$$\frac{d^2\sigma}{p_c^2 dp_c d\Omega_c} = N \exp\left(-\frac{p_c^2}{2\sigma^2}\right), \tag{4}$$

where p_c is the momentum of the neutron in the rest frame of the source and σ is a width parameter that is related to the internal momentum of nucleons within the source [41].

The double-differential spectra reported here are related to the cross section in Eq. (3) by

$$\frac{d^2\sigma}{dEd\Omega} = pE_c \frac{d^2\sigma}{p_c^2 dp_c d\Omega_c}, \tag{5}$$

where E_c is the neutron's kinetic energy in the source's frame, and p is the neutron's momentum in the lab frame. E_c is related to the kinetic energy in the lab frame by

$$E_c = \gamma(E - \beta p \cos\theta), \tag{6}$$

where β is the source velocity (v/c), γ is the Lorentz factor, and θ is the lab angle.

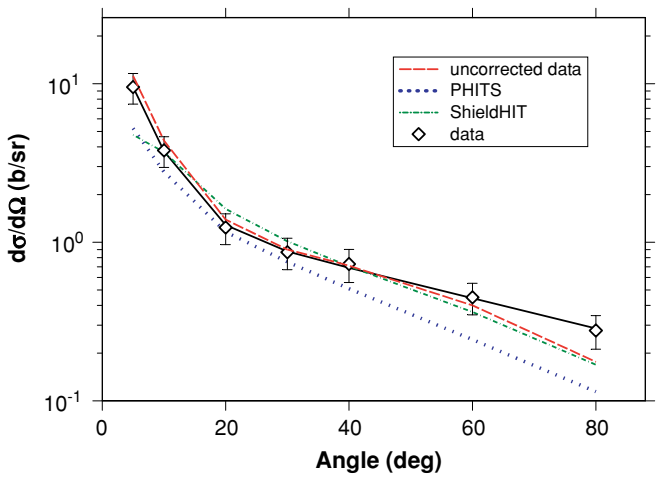

FIG. 8. (Color online) Angular distribution for the 290 MeV/nucleon C + marsbar system. The data are shown with the symbols. The error bars include both systematic and statistical uncertainties. The dashed (red) line shows the data without corrections for attenuation and for production from nontarget materials. Results from PHITS and SHIELD-HIT calculations are shown with the dotted (blue) and dot-dashed (green) lines, respectively. The solid line comes from a fit explained in the text.

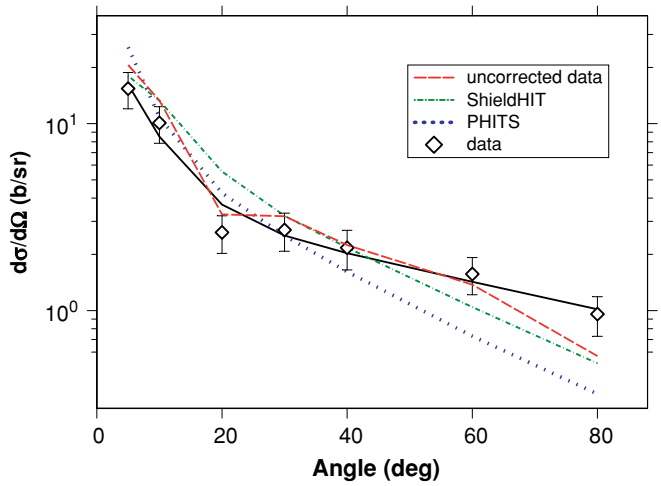

FIG. 9. (Color online) Angular distribution for the 400 MeV/nucleon Ne + ISS wall system. The data are shown with the symbols. The error bars include both systematic and statistical uncertainties. The dashed (red) line shows the data without corrections for attenuation and for production from nontarget materials. Results from PHITS and SHIELD-HIT calculations are shown with the dotted (blue) and dot-dashed (green) lines, respectively. The solid line comes from a fit explained in the text.

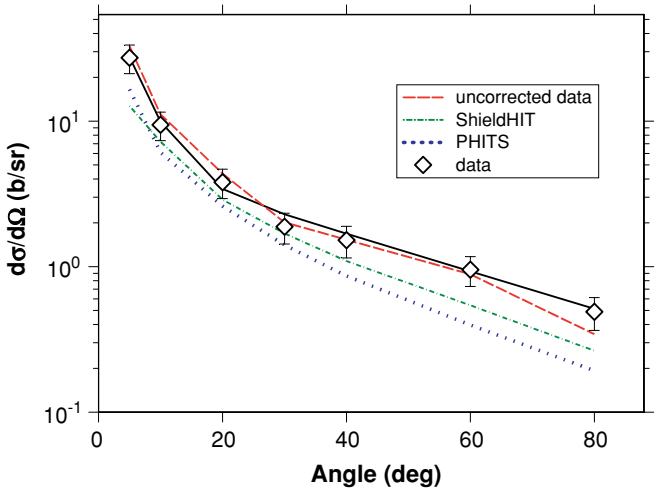

FIG. 10. (Color online) Angular distribution for the 600 MeV/nucleon Ne + marsbar system. The data are shown with the symbols. The error bars include both systematic and statistical uncertainties. The dashed (red) line shows the data without corrections for attenuation and for production from nontarget materials. Results from PHITS and SHIELD-HIT calculations are shown with the dotted (blue) and dot-dashed (green) lines, respectively. The solid line comes from a fit explained in the text.

If one assumes an isotropic decay in their rest frame the other two sources are given by the following Maxwellian form (in the rest frame):

$$\frac{d^2\sigma}{p_c^2 dp_c d\Omega_c} = \frac{N}{(2\pi T)^{3/2}} \exp\left(-\frac{p_c^2}{2mT}\right). \quad (7)$$

Table VII shows the fit parameters from all three systems. The utility of the moving-source model is that it provides a good parametrization of the data. However, it should be cautioned that the set of fitted parameters is not a unique solution, and as such no attempt should be made to extrapolate the values listed in Table VII to model other systems involving other projectiles, projectile energies, or targets.

In general, the moving-source parametrization does a good job in reproducing the data. The parameters extracted here follow the general trends of the parameters reported in Ref. [34], with the notable exception of the width parameter (σ) extracted from the fit to the 290 MeV/nucleon C + marsbar system. The value of that width parameter is lower than other reported values, and it is lower than what is expected from the distribution of momenta arising from the internal motion of nucleons within the nucleus.

B. Transport model calculations

Transport model calculations are capable of tracking primary radiation fields as they slow down or break up in complex shielding configurations. All secondary particles produced by nuclear interactions are tracked as well, leading to a well-defined description of the radiation field in or beyond shielding. The two models used here to compare with the measured data transport the primary beam through the beam exit window, beam scintillator, target, and air gap, producing neutrons in any of those materials. After neutrons are produced, they are transported through any intervening materials between the point of production and the neutron detector. Consequently, a more meaningful comparison between the data and transport model calculations involves the data before any corrections for neutron production in nontarget materials that are shadowed by the shadow bars, or for neutron attenuation in the intervening materials. Thus, when comparing transport model calculations with the data in Figs. 5–10, the comparisons should be made with the solid red lines that represent the data before the corrections previously mentioned.

1. SHIELD-HIT model calculations

The code SHIELD-HIT [42] is an adaptation of the general-purpose code SHIELD. It simulates the interactions of hadrons and atomic nuclei of arbitrary charge and mass number (Z, A) with complex extended targets in an energy range from 1 TeV/nucleon down to 1 MeV/nucleon, and to thermal energies in the case of neutrons.

Nuclear reactions in SHIELD-HIT are simulated using Russian nuclear models where all stages of hadron-nucleus and nucleus-nucleus inelastic interaction are described, keeping track of the generation and transport of all types of secondary particles down to the cutoff energy of the simulation process. SHIELD-HIT describes inelastic nuclear reactions using the many stage dynamical model (MSDM) [43]. The MSDM assumes that inelastic nuclear interactions proceed through the following subsequent stages: fast cascade, coalescence, pre-equilibrium decay of residual nuclei, and, finally, equilibrated de-excitation of a nucleus. The fast cascade stage of nuclear reactions reduces the projectile-target interaction to a series of binary collisions between nuclear constituents and/or produced hadrons. Below 1 GeV this stage is modeled using the Dubna cascade model [44]. At the end of the cascade stage, nucleons that are close to each other in momentum space can coalesce to form complex particles such as ^{2}H, ^{3}H, ^{3}He nuclei, and α particles [44]. Evolution of the excited residual nucleus toward equilibrium is described in terms of the

TABLE V. Fit parameters for the angular distributions from all three systems, using Eq. (3). The units for a_1 and a_3 are b/sr, and the units for a_2 and a_4 are deg^{-1}.

System	a_1	a_2	a_3	a_4
290 C + marsbar	26.9 ± 1.1	0.241 ± 0.007	1.66 ± 0.08	0.0219 ± 0.0009
400 Ne + ISS wall	30.6 ± 2.0	0.177 ± 0.011	3.9 ± 0.3	0.0169 ± 0.0012
600 Ne + marsbar	90. ± 5.	0.274 ± 0.012	5.5 ± 0.3	0.0297 ± 0.0010

TABLE VI. Total cross sections above 3 MeV, integrated between 0° and 90°, from all three systems. The second column shows the total cross sections for the corrected data. The third column displays the total cross sections converted to units of number of neutrons/incoming ion/g-cm^2 of material. The fourth column displays the total cross sections for data not corrected for neutron attenuation and for neutron production in nontarget materials. The results from transport model calculations (fifth and sixth columns) should be compared with the uncorrected data.

System	σ(b)	Neutrons/ion/(g/cm^2)	Uncorrected σ (b)	SHIELD-HIT (b)	PHITS (b)
290 MeV/nucleon C + marsbar	4.3 ± 0.4	0.18 ± 0.02	4.2 ± 0.4	3.8	2.8
400 MeV/nucleon Ne + ISS wall	12.3 ± 1.2	0.26 ± 0.03	12.7 ± 1.2	12.4	10.0
600 MeV/nucleon Ne + marsbar	10.3 ± 0.9	0.43 ± 0.04	10.6 ± 0.9	6.6	5.7

pre-equilibrium model based on a Monte Carlo solution of the corresponding master equation [45]. In this stage nucleons and light nuclei ($A < 16$) can be emitted during the equilibration process. Further equilibrated de-excitation of the residual nucleus is included through several mechanisms. For light nuclei a modified model of the Fermi breakup [43] is used. Medium and heavy nuclei under moderate excitation ($E^*/A < 2$ MeV) suffer successive particle evaporation, including competition of evaporation and fission for heavy nuclei [43,46]. Highly excited nuclei ($E^*/A > 2$ MeV) can be disintegrated into several excited fragments according to the statistical model of multifragmentation (SMM) [47] with subsequent emission of particles from the fragments.

In the default output of SHIELD-HIT, spatial distributions of the energy deposition from ionization losses of heavy charged particles—such as primary particles, nuclear fragments, recoil nuclei, and charged secondary particles from neutron interactions—are scored. An accurate track-length algorithm for the evaluation of the fluence differential in energy, of both the primary ions and their secondaries, including higher order generations of all particles, at selected regions (zones) in the simulated geometry has been implemented. In addition, the energy spectra of the secondary neutrons produced inside the geometry and the decelerated spectra of neutrons transported through and flying out from the geometry can be scored, providing useful data for radiation protection aspects of heavy-ion beam irradiation. For neutrons leaving the geometry, the spectra differential in both energy and angle are evaluated.

SHIELD-HIT calculations of the double-differential spectra from all three systems are shown with the dashed (green online) histograms in Figs. 5–7. The statistical uncertainties in the calculations are less than 10%. In general, the calculations do an excellent job in reproducing the spectral shapes shown with the dashed (red online) lines at each angle in all three systems, although the magnitudes of the calculated spectra are generally lower than the measured magnitudes. SHIELD-HIT calculations of the yields above 3 MeV at each angle are shown with the dot-dashed (green online) lines in Figs. 8–10. The relevant data to compare with are shown with the dashed (red online) lines. At 5°, SHIELD-HIT underestimates the yield by over a factor of 2 in both systems that used the marsbar target. The calculated yields at 80° are underestimated in all three systems. At most other angles, the calculated yields are in general agreement with the data, and in some cases (notably the 290 MeV/nucleon C system) the agreement is excellent. Calculated total yields above 3 MeV and integrated between 0° and 90° are within 10% of the experimental yields for the 290 and 400 MeV/nucleon systems (see Table VI). Agreement with the experimental total yield for the 600 MeV/nucleon system is worse; the calculated yield is 40% lower than the measured yield. In all three systems, the calculated yields are less than the measured yields.

2. PHITS model calculations

The heavy-ion transport code PHITS (particle and heavy ion transport code system) [17] is based on the NMTC/JAM code [48]. NMTC/JAM is a nucleon and meson transport code that uses the high-energy nucleon-nucleus reaction code JAM [49] for the intranuclear cascade calculation and GEM [50]

TABLE VII. Moving-source model fit parameters for the given systems. Source 1 is the projectile source, source 2 is the overlap-region source, and source 3 is the target-remnant source.

		290 C + marsbar	400 Ne + ISS wall	600 Ne + marsbar
Source 1	N (b)	$(1.44 \pm 0.04) \times 10^{-7}$	$(1.24 \pm 0.06) \times 10^{-7}$	$(1.20 \pm 0.03) \times 10^{-7}$
	σ(MeV/c)	63.0 ± 0.7	86.5 ± 1.9	98.6 ± 1.0
	β	0.598 ± 0.001	0.673 ± 0.002	0.756 ± 0.001
Source 2	N (b)	2.66 ± 0.05	9.9 ± 0.3	7.53 ± 0.14
	T (MeV)	51.6 ± 0.6	82.2 ± 1.3	99 ± 2
	β	0.346 ± 0.005	0.29 ± 0.01	0.36 ± 0.01
Source 3	N (b)	1.72 ± 0.06	5.1 ± 0.3	3.01 ± 0.14
	T (MeV)	10.4 ± 0.6	4.0 ± 0.5	7.3 ± 0.6
	β	0.000 ± 0.002	0.000 ± 0.001	0.000 ± 0.001

for the evaporation and fission processes. To extend the capabilities of NMTC/JAM to include heavy-ion transport, PHITS uses Shen's formula [51] to calculate the heavy-ion total-reaction cross section, the SPAR code [52] to calculate the stopping powers and ranges, and JQMD [53] to simulate heavy-ion nuclear interactions. JQMD is based on the QMD model in which nuclei are described as a self-binding system of nucleons that are interacting with each other within the framework of molecular dynamics. PHITS is a sophisticated simulation code, containing many built-in tallies commonly used for studying radiation effects, such as track length, surface crossing, heat deposition, displacements per atom, "star," and reaction product yields. Both the Complex Geometry (CG) system (typically used in HETC, LAHET, and NMTC calculations) and the General Geometry (GG) system (used in MCNP calculations) are available for use in PHITS.

PHITS calculations of the double-differential spectra from all three systems are shown with the solid (blue online) histograms in Figs. 5–7. As with the SHIELD-HIT calculations, the PHITS calculations do an excellent job in reproducing the spectral shapes shown with the dashed (red online) lines at each angle in all three systems. The magnitudes of the calculated PHITS spectra are generally lower than the measured magnitudes. PHITS calculations of the yields above 3 MeV at each angle are shown with the dotted (blue online) lines in Figs. 8–10. The relevant data to compare with are shown with the dashed (red online) lines. At 5°, PHITS calculations underestimate the yield in both systems that used the marsbar target, although they are somewhat closer to the measured values than the corresponding SHIELD-HIT calculations. At most angles, the calculated yields are in general agreement with the measured values. Calculated total yields above 3 MeV and integrated between 0° and 90° are within 30% of the experimental yields for the 290 MeV/nucleon system, 20% of those for the 400 MeV/nucleon system, and 45% of those for the 600 MeV/nucleon system (see Table VI). Comparisons of PHITS calculations with double-differential neutron spectra from 290 MeV/nucleon C interacting in a carbon target [17] show much better agreement with the data than is observed here with the 290 MeV/nucleon C + marsbar system. One possible explanation may be the thickness of the marsbar target. Whereas PHITS calculations of thin-target cross sections are in excellent agreement, the calculations of stopping target neutron yields [17] typically underestimate the measured yields, especially at forward angles. The marsbar target used here is much thicker (5 g/cm$^{2)}$ than the targets used in the 290 MeV/nucleon C + C measurement (1.8 g/cm^2) [34]. The underestimation of the data observed here may be indicative of a trend with PHITS calculations and the thickness of the target. It is interesting to note that the best agreement between PHITS and data is with the thinnest target (2.97 g/cm^2 ISS wall, which is still thicker than the carbon target used in the previous measurement).

VI. SUMMARY

Double-differential secondary neutron-production cross sections from 290 MeV/nucleon C + marsbar (a composite material made of simulated Martian regolith and polyethylene), 600 MeV/nucleon Ne + marsbar, and 400 MeV/nucleon Ne + ISS wall (a section of wall material from the International Space Station) have been measured. The data were corrected for neutron flux attenuation in intervening materials and for the production of neutrons by materials near the target location. At 5°, the most forward measurement in the laboratory, the spectra show a strong contribution from projectile fragmentation, resulting in a peak in the distribution centered about the mean beam energy (per nucleon) in the target. Broader, less pronounced peaks caused by projectile fragmentation can also be seen at 10° and 20°, but it is at these angles where the decay of the overlap region between the target and projectile begins to dominate the spectra. At the most backward angles measured (60° and 80°) the effects of target evaporation are evidenced by the exponential behavior of the spectra for neutron energies less than 50 MeV. Angular distributions and total production cross sections for neutron energies above 3 MeV were also extracted from the data. Also shown were the data without corrections for neutron flux attenuation through the target and for neutron production in nontarget materials. Comparisons of the uncorrected data with SHIELD-HIT and PHITS Monte Carlo calculations show that the codes do an excellent job of reproducing the spectral shapes at each angle, for all three systems. The calculations of the uncorrected angular yields underestimate the data, in general, although in some cases the agreement is very good. Both codes show that the calculated magnitudes of the total uncorrected yields are underestimated by 10–45%.

ACKNOWLEDGMENTS

The experimental program was carried out as part of a research project with heavy ions at NIRS-HIMAC. The authors wish to thank Michiya Sasaki, Hiroshi Yashima, Taishi Shiomi, and Yuuichi Tozawa for their help during the experiments. The authors also wish to thank the staff of HIMAC for their invaluable assistance during the experiment. This research was supported in part by the U.S. Department of Energy under Contract No. DEAC03076SF00098, the National Aeronautics and Space Administration under NASA Grant Nos. L14230C and H29456D, and the Japanese Society for the Promotion of Science (JSPS) under Grant No. US02011.

[1] Report 98, "Guidance on Radiation Received in Space Activities," National Council on Radiation Protection and Measurements, NCRP Publications, 7910 Woodmont Ave., Suite 400, Bethesda MD (1989).

[2] Report 132, "Radiation Protection Guidance for Activities in Low Earth Orbit," National Council on Radiation Protection and Measurements, NCRP Publications, 7910 Woodmont Ave., Suite 400, Bethesda MD (2000).

[3] L. C. Simonsen and J. E. Nealy, Technical Paper 3079, National Aeronautics and Space Administration, 1991.

[4] E. V. Benton and G. D. Badhwar, eds., Radiat. Meas. **33**, 227 (2001).

[5] J. W. Wilson, L. W. Townsend, H. B. Bidasaria, W. Schimmerling, M. Wong, and J. Howard, Health Phys. **46**, 1101 (1984).
[6] J. W. Wilson, M. Reginato, F. Hajnal, and S. Y. Chun, Health Phys. **68**, 532 (1995).
[7] J. W. Wilson, R. K. Tripathi, G. D. Qualls, F. A. Cucinotta, R. E. Prael, J. W. Norbury, J. H. Heinbockel, J. Tweed, and G. De Angelis, Radiat. Res. **43**, S87 (2002).
[8] J. W. Wilson, F. F. Badavi, F. A. Cucinotta, J. L. Shinn, G. D. Badhwar, R. Silberger, C. H. Tsao, L. W. Townsend, and R. K. Tripathi, NASA Technical Paper 3495, 1995.
[9] T. W. Armstrong and K. G. Chandler, Nucl. Sci. Eng. **49**, 110 (1972).
[10] N. M. Sobolevsky, Report JINR B1-2-5458 Dubna 1-143, 1970 (in Russian).
[11] H. W. Bertini, Phys. Rev. **188**, 1711 (1969).
[12] V. S. Barashenkov and V. D. Toneev, *Interactions of High Energy Particles and Atomic Nuclei with Nuclei* (Atomizdat, Moscow, 1972) (in Russian).
[13] P. Cloth, D. Filges, R. D. Neef, G. Sterzenbach, Ch. Reul, T. W. Armstrong, B. L. Colborn, B. Anders, and H. Brückmann, KFA-Report Jül-2203, 1988 (unpublished).
[14] R. E. Prael and H. Lichtenstein, Los Alamos National Laboratory LA-UR-89-3014, 1989.
[15] G. Hughes, K. J. Adams, M. B. Chadwick, J. C. Comly, S. C. Frankle, J. S. Hendricks, R. C. Little, R. E. Prael, L. S. Waters, and P. G. Young Jr., in *Proceedings of Third Workshop on Simulating Accelerator Radiation Environments (SARE 3) KEK, Tsukuba, Japan, May 7–9*, edited by H. Hirayama, KEK Proceedings 97-5, H/R/D, 1997, p. 44.
[16] H. Takada, N. Yoshizawa, K. Kosaka, and K. Ishibashi, JAERI-Data/Code 98-005, 1998.
[17] H. Iwase, K. Niita, and T. Nakamur, J. Nucl. Sci. Technol. **39**, 1142 (2002).
[18] K. Niita, T. Sato, H. Iwase, H. Nose, H. Nakashima, and L. Sihver, in Proceedings; 2003 Symposium on Nuclear Data, Nov. 2003, JAERI, Takai, Japan, JAERI-Conf2004-005, 2004, p. 33.
[19] N. V. Mokhov, Fermilab-FN-628, 1995.
[20] A. Fassò, A. Ferrari, J. Ranft, and P. R. Sala, in *Proceedings of Third Workshop on Simulating Accelerator Radiation Environments (SARE 3) KEK, Tsukuba, Japan, May 7–9,* edited by H. Hirayama KEK Proceedings 97-5, H/R/D, 1997.
[21] A. Ferrari and P. R. Sala, in *International Conference on Nuclear Data for Science and technology, Miramare-Trieste, Italy, May 19–24,* edited by G. Reffo, A. Ventura, and C. Grandi, 1997, p. 247.
[22] R. Brun, R. Hagelberg, M. Hansroul, and J. C. Lassale, CERN DD/78/2, 1978.
[23] R. A. Cecil, B. D. Anderson, A. R. Baldwin, R. Madey, A. Galonsky, P. Miller, L. Young, and F. M. Waterman, Phys. Rev. C **21**, 2471 (1980).
[24] T. Kurosawa, N. Nakao, T. Nakamura, Y. Uwamino, T. Shibata, N. Nakanishi, A. Fukumura, and K. Murakami, Nucl. Sci. Eng. **132**, 30 (1999).
[25] T. Kurosawa, N. Nakao, T. Nakamura, Y. Uwamino, T. Shibata, A. Fukumura, and K. Murakami, J. Nucl. Sci. Technol. **36**, 41 (1999).
[26] T. Kurosawa, N. Nakao, T. Nakamura, H. Iwase, H. Sato, Y. Uwamino, and A. Fukumura, Phys. Rev. C **62**, 044615 (2000).
[27] L. Heilbronn, R. S. Cary, M. Cronqvist, F. Deak, K. Frankel, A. Galonsky, K. Holabird, A. Horvath, A. Kiss, J. Kruse, R. M. Ronningen, H. Schelin, Z. Seres, C. E. Stronach, J. Wang, P. Zecher, and C. Zeitlin, Nucl. Sci. Eng. **132**, 1 (1999).
[28] B. I. Britvich, A. A. Chumakov, R. M. Ronningen, R. A. Blue, and L. H. Heilbronn, Rev. Sci. Instrum. **70**, 2314 (1999).
[29] W. Schimmerling, J. W. Kast, D. Ortendahl, R. Madey, R. A. Cecil, B. D. Anderson, and A. R. Baldwin, Phys. Rev. Lett. **43**, 1985 (1979).
[30] R. A. Cecil, B. D. Anderson, A. R. Baldwin, R. Madey, W. Schimmerling, J. W. Kast, and D. Ortendahl, Phys. Rev. C **24**, 2013 (1981).
[31] R. Madey, B. D. Anderson, R. A. Cecil, P. C. Tandy, and W. Schimmerling, Phys. Rev. C **28**, 706 (1983).
[32] A. R. Baldwin, R. Madey, W. M. Zhang, B. D. Anderson, D. Keane, J. Varga, J. W. Watson, G. D. Westfall, K. Frankel, and C. Gale, Phys. Rev. C **46**, 258 (1992).
[33] H. Sato, T. Kurosawa, H. Iwase, T. Nakamura, Y. Uwamino, and N. Nakao, Phys. Rev. C **64**, 034607 (2001).
[34] Y. Iwata, T. Murakami, H. Sato, H. Iwase, T. Nakamura, T. Kurosawa, L. Heilbronn, R. M. Ronningen, K. Ieki, Y. Tozawa, and K. Niita, Phys. Rev. C **64**, 054609 (2001).
[35] J. H. Heltsley, L. Brandon, A. Galonsky, L. Heilbronn, B. A. Remington, S. Langer, A. Vandermolen, and J. Yurkon, Nucl. Instrum. Methods A **263**, 441 (1988).
[36] L. Heilbronn, Y. Iwata, and H. Iwase, Nucl. Instrum. Methods A **522**, 495 (2004).
[37] R. A. Cecil, B. D. Anderson, and R. Madey, Nucl. Instrum. Methods **161**, 439 (1979).
[38] L. H. Heilbronn, Ph.D. thesis, Michigan State University, 1991.
[39] N. Nakao, T. Nakamura, M. Baba, Y. Uwamino, N. Nakanishi, H. Nakashima, and S. Tanaka, Nucl. Instrum. Methods Phys. Res. A **362**, 454 (1995).
[40] R. Wallace, Nucl. Instrum. Methods **18**, 405 (1962).
[41] R. Serber, Phys. Rev. **72**, 1008 (1947).
[42] I. Gudowska, N. M. Sobolevsky, P. Andreo, D. Belkić, and A. Brahme, Phys. Med. Biol. **49**, 1933 (2004).
[43] A. S. Botvina, A. S. Iljinov, I. N. Mishustin, J. P. Bondorf, R. Donangelo, and K. Sneppen, Nucl. Phys. **A475**, 663 (1987).
[44] V. D. Toneev and K. K. Gudima, Nucl. Phys. **A400**, 173c (1983).
[45] K. K. Gudima, S. G. Mashnik, and V. D. Toneev, Nucl. Phys. **A401**, 329 (1983).
[46] G. D. Adeev, A. S. Botvina, A. S. Iljinov, M. V. Mebel, N. I. Pischasov, and O. I. Serdyuk, Preprint INR RAS 0816/93 Moscow, 1-24, 1993 (in Russian).
[47] A. S. Botvina, A. S. Iljinov, and I. N. Mishustin, Nucl. Phys. **A507**, 649 (1990).
[48] K. Niita, H. Takada, S. Meigo, and Y. Ikeda, Nucl. Instrum. Methods B **184**, 406 (2001).
[49] Y. Nara, N. Otuka, A. Ohnishi, K. Niita, S. Chiba, Phys. Rev. C **61**, 024901 (1999).
[50] S. Furihata, Nucl. Instrum. Methods B **171**, 251 (2000).
[51] S. Wen-qing, W. Bing, F. Jun, Z. Wen-long, Z. Yong-tai, and F. En-pu, Nucl. Phys. **A491**, 130 (1989).
[52] T. W. Armstrong, K. C. Chandler, ORNL-4869, Oak Ridge National Laboratory, 1973.
[53] K. Niita, S. Chiba, T. Maruyama, T. Maruyama, H. Takada, T. Fukahori, Y. Nakahara, and A. Iwamoto, Phys. Rev. C **52**, 2620 (1995).